AIAA JOURNAL
Vol. 33, No. 7, July 1995

Large-Eddy Simulation of Turbulent Anisochoric Flows

C. Fureby*
Lund Institute of Technology, S-22100 Lund, Sweden

The objective of this study is to develop a large eddy simulation model for nonreacting as well as chemically reacting flows at high Reynolds numbers. This paper focuses on the large eddy simulation model applied to the nonreacting case and the evaluation of its predictive capabilities. Further, results from the large eddy simulations are used to investigate the large-scale structures present in unsteady wake flows. The large eddy simulation model contains subgrid-scale models for both cross and Reynolds quantities to account for both outscatter (i.e., transfer from small scales to larger scales) transfer between large scales and dissipation. To evaluate the large eddy simulation model, results from two- and three-dimensional large eddy simulations of nonreacting flow in a rectilinear channel with a triangular shaped bluff body are compared with experimental measurements and with results from two-dimensional simulations made with the k–ε model and a differential Reynolds stress model. The investigations indicate that the results obtained with the large eddy simulation model is in good agreement with experimental data. Comparison of results obtained with the large eddy simulation model and results obtained with the k–ε model and the differential Reynolds stress model clearly reveals the known weaknesses of the latter methods.

Introduction

DIRECT numerical simulation (DNS) of turbulent flows at high Reynolds (Re) number encountered in problems of technological importance is almost impossible since energy containing eddies of a wide range of sizes are present. If it was possible to solve the set of conservation and balance equations for mass, momentum, and energy exactly, turbulence would appear naturally in the solutions. Traditional simulation models based on Reynolds averages (RAS) have had only limited success since the large eddies, which contain most of the energy, are highly dependent on the geometry of the flow. Experience has indicated that such models usually break down when a variety of turbulent flows are considered.[1] The small scales are assumed more universal in character, and serve mainly as a source for dissipation. Hence, it can be argued that more accurate simulations could be achieved if only the small eddies are modeled while the motion of the large eddies are simulated.[2]

The notation anisochoric is used herein in the sense as expressed by Truesdell[3]:

> Writers on hydrodynamics are guilty of propagating not only bad English but also confusion when they refer to incompressible flows." A flow, obviously, cannot be compressed. A flow may or may not be isochoric, and a fluid may or may not be incompressible; the behavior of an incompressible fluid in a certain, necessarily isochoric flow is generally not at all the same as that of any compressible fluid in the same isochoric flow.

During the past decade, considerable progress has been made in the use of large eddy simulations (LES) for isochoric (i.e., volume preserving) turbulent flows. This effort has shed new light on the physics of turbulence. Despite the intensive research effort devoted to LES of isochoric flows it appears that only few LES of anisochoric flows[2] have been attempted. Undoubtedly, technological applications, such as turbulent supersonic flows including shock waves and combustion, where there is the strong interaction between the energy release from chemical reactions and the dynamics of fluid motion, are of great importance. The prerequisite for carrying out such computations is the development of suitable subgrid-scale (SGS) models for anisochoric flows. With the exception of the works in Refs. 4–7 few studies along these lines have been published.

The objective of this study is to develop an LES model that can be used for simulating both nonreacting and chemically reacting flows at high Re numbers. Such simulation models can give detailed insight into the physics behind turbulent combustion as well as be used to improve design of different applications like IC engines, jet engines, and pulse combustors. This paper focuses on describing the LES model for the nonreacting case and evaluating its predictive capabilities by comparing simulation results with experimental measurements. Simulation results from traditional RAS methods like the k–ε model and a differential Reynolds stress model (DRSM) are presented for comparison. Further, results from the LESs are used to investigate and characterize the mechanism behind the large-scale structure in unsteady wake flow.

The object, on which numerical simulations and measurements have been carried out, is a model of an afterburner of a jet engine, described in Ref. 8. The rig consists of a rectilinear channel with rectangular cross section. At the location of one-third of the channel length downstream from the inlet section, a two-dimensional triangular shaped bluff body is located, see Fig. 1. The flow past bluff bodies has been the subject of many papers of both experimental and theoretical nature,[9–11] and, therefore, knowledge of the flow structure and how traditional simulation models capture the flowfield is available.

Numerical simulations with the presented LES model have been carried out for nonreacting flows at Re numbers between 10^3 and 10^5 and Mach numbers Ma between 0.01 and 0.20. The results from the LES model are postprocessed in order to obtain statistical information and statistical moments that are compared with measured quantities. The examinations indicate that the results obtained with the LES model, even the two-dimensional LES model, are in better agreement with results from experimental measurements than are the results obtained with the k–ε model and the DRSM.

Governing Equations of Fluid Dynamics

In mechanics the same physical laws govern all material bodies; these general laws in continuum physics are expressed as balance or conservation laws.[12] More precisely, the physical laws assert that we always will have balance of mass, momentum, and energy and imbalance of entropy. Thus,

$$\partial_t(\rho) + \mathrm{div}(\rho\dot{\boldsymbol{x}}) = 0 \tag{1a}$$

$$\partial_t(\rho\dot{\boldsymbol{x}}) + \mathrm{div}(\rho\dot{\boldsymbol{x}} \otimes \dot{\boldsymbol{x}}) = \mathrm{div}\boldsymbol{T} + \rho\boldsymbol{b} \tag{1b}$$

$$\partial_t(\rho e) + \mathrm{div}(\rho e\dot{\boldsymbol{x}}) = \boldsymbol{T} \cdot \boldsymbol{L} + \mathrm{div}\boldsymbol{h} + \rho\sigma \tag{1c}$$

$$\rho\dot{\eta} \geq \mathrm{div}(\boldsymbol{h}/\theta) + \rho\sigma/\theta \tag{1d}$$

where ρ is the density, $\dot{\boldsymbol{x}}$ the velocity, $\boldsymbol{T}$ the stress tensor, $\boldsymbol{b}$ the specific body force, e the specific internal energy, and $\boldsymbol{L}$ the velocity

Received May 13, 1994; revision received Nov. 4, 1994; accepted for publication Jan. 10, 1995.

*Professor, Department of Combustion Physics, Box 118.

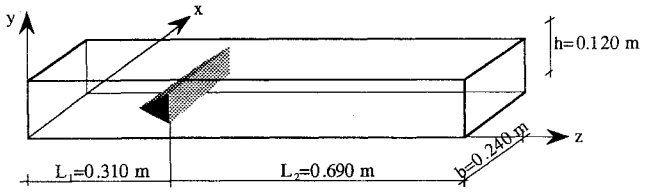

Fig. 1 Validation rig outline, coordinate system, and overall dimensions.

gradient. $\boldsymbol{T} \cdot \boldsymbol{L}$ is the net power which, since $\boldsymbol{T}$ is symmetric, also can be written in the form $\boldsymbol{T} \cdot \boldsymbol{D}$, where $2\boldsymbol{D} = (\boldsymbol{L} + \boldsymbol{L}^T)$ is the rate of strain tensor. Also, $\boldsymbol{h}$ is the heat conduction vector, σ the specific radiation, η the specific entropy, and θ is the temperature. The conservation and balance equations (1) are themselves insufficient to determine the flow, thus, before we can formulate a determinate problem, it is necessary to introduce constitutive equations; we will assume the special case of a linear viscous fluid with Fourier heat conduction,

$$e = e(\theta, \rho), \qquad \eta = \eta(\theta, \rho)$$

$$\boldsymbol{h} = \kappa \ \text{grad}\,\theta \tag{2}$$

$$\boldsymbol{T} = -p\boldsymbol{I} + \boldsymbol{S} = -p\boldsymbol{I} + \lambda(\text{tr}\,\boldsymbol{D})\boldsymbol{I} + 2\mu\boldsymbol{D}$$

where p is the thermodynamic pressure and $\boldsymbol{S}$ is the viscous stress tensor whereas $\kappa = \kappa(\rho, \theta)$, $\lambda = \lambda(\rho, \theta)$, and $\mu = \mu(\rho, \theta)$ are the heat conductivity and the coefficients of viscosity. Further, to satisfy the entropy inequality (1d) the restrictions $2\lambda + 3\mu \geq 0$, $\mu \geq 0$, and $\kappa \geq 0$ must be satisfied. When dealing with compressible fluids it is often practical to introduce the total specific energy $E = e + \frac{1}{2}(\dot{\boldsymbol{x}} \cdot \dot{\boldsymbol{x}})$ or the specific enthalpy $h = e + p/\rho$ instead of the specific internal energy. Using the specific enthalpy we find

$$\partial_t(\rho) + \text{div}(\rho\dot{\boldsymbol{x}}) = 0$$

$$\partial_t(\rho\dot{\boldsymbol{x}}) + \text{div}(\rho\dot{\boldsymbol{x}} \otimes \dot{\boldsymbol{x}}) = -\text{grad}\,p + \text{div}\boldsymbol{S} + \rho\boldsymbol{b} \tag{3}$$

$$\partial_t(\rho h) + \text{div}(\rho h\dot{\boldsymbol{x}}) = \dot{p} + \boldsymbol{S} \cdot \boldsymbol{D} + \text{div}\,\boldsymbol{h} + \rho\sigma$$

where $\dot{p} = \partial_t(p) + \dot{\boldsymbol{x}} \cdot \text{grad}\,p$ is the substantial time derivative of pressure. The flow medium is here assumed to follow the ideal gas law: $p = \rho R\theta$ and the state equation $h = C_p(\theta - \theta_0)$ where R is the universal gas constant and C_p is the specific heat at constant pressure.

Reynolds Average Simulations

Since the early work of Taylor,[13] statistical methods such as RAS have been employed for alleviating the computational requirements of DNS. The motivation for describing turbulence in a statistical sense stems from the speculation that at high Re numbers average values are weak functions of the Re number.[14] Therefore, an alternative way of describing the structure of turbulent flows is to construct equations for some statistical average. More precisely, any flow variable ϕ can be decomposed into ensemble average and fluctuating parts as follows:

$$\phi = \bar{\phi} + \phi', \qquad \bar{\phi} = \lim_{N > N_0} \frac{1}{N} \sum_{\alpha=1}^{N} (\phi)^\alpha$$

$$\phi = \tilde{\phi} + \phi'', \qquad \overline{\rho\phi} = \bar{\rho}\tilde{\phi} = \lim_{N > N_0} \frac{1}{N} \sum_{\alpha=1}^{N} (\rho\phi)^\alpha \tag{4}$$

where N_0 is a sufficiently large number of realizations. Ensemble averaging the fluid dynamics equations (1–3) yields the following set of governing equations for the ensemble averaged variables:

$$\partial_t(\bar{\rho}) + \text{div}(\bar{\rho}\tilde{\dot{\boldsymbol{x}}}) = 0$$

$$\partial_t(\bar{\rho}\tilde{\dot{\boldsymbol{x}}}) + \text{div}(\bar{\rho}\tilde{\dot{\boldsymbol{x}}} \otimes \tilde{\dot{\boldsymbol{x}}}) = -\text{grad}\,\bar{p} + \text{div}(\bar{\boldsymbol{S}} - \boldsymbol{R}) + \bar{\rho}\tilde{\boldsymbol{b}} \tag{5}$$

$$\partial_t(\bar{\rho}\tilde{h}) + \text{div}(\bar{\rho}\tilde{h}\tilde{\dot{\boldsymbol{x}}}) = \bar{\dot{p}} + \overline{\boldsymbol{S} \cdot \boldsymbol{D}} + \text{div}(\bar{\boldsymbol{h}} - \boldsymbol{r}) + \bar{\rho}\bar{\sigma}$$

The averaging procedure results in "smoothing" the fluid dynamic equations and the physical variables so that they can be represented on a given computational mesh. The ensemble averaged equations contain additional terms, the density weighted Reynolds stresses $\boldsymbol{R}$ and fluxes $\boldsymbol{r}$,

$$\boldsymbol{R} = \bar{\rho}(\widetilde{\dot{\boldsymbol{x}}'' \otimes \dot{\boldsymbol{x}}''}), \qquad \boldsymbol{r} = \bar{\rho}(\widetilde{h''\dot{\boldsymbol{x}}''}) \tag{6}$$

resulting from the nonlinearities in the convective terms of the fluid dynamic equations. In Eq. (5) the average thermodynamic pressure is given by $\bar{p} = \bar{\rho}R\tilde{\theta}$. In virtually all existing RAS it is assumed that fluctuations in the thermal conductivity and in the viscosities can be neglected in the flow except for a thin sublayer near the wall. This results in the following approximate expressions for the heat conduction vector and the viscous stress tensor:

$$\bar{\boldsymbol{h}} = \overline{\kappa \ \text{grad}\,\theta} \approx \bar{\kappa} \ \text{grad}\,\tilde{\theta} = (\bar{\kappa}/\bar{C}_p)\text{grad}\,\tilde{h}$$

$$\bar{\boldsymbol{S}} = \overline{\lambda \ \text{tr}\,(\boldsymbol{D})\boldsymbol{I} + 2\mu\boldsymbol{D}} \approx \bar{\lambda} \ \text{tr}\,(\tilde{\boldsymbol{D}})\boldsymbol{I} + 2\bar{\mu}\tilde{\boldsymbol{D}} \tag{7}$$

where the following approximations are adopted: $\bar{\kappa} = \kappa(\bar{\rho}, \tilde{\theta})$, $\bar{C}_p = C_p(\tilde{\theta})$, $\bar{\mu} = \mu(\bar{\rho}, \tilde{\theta})$, and $\bar{\lambda} = \lambda(\bar{\rho}, \tilde{\theta})$. The dissipation function and the substantial time derivative of pressure can, with the aid of Eq. (7) and a relation between density weighted and unweighted averages, be rewritten according to

$$\overline{\boldsymbol{S} \cdot \boldsymbol{D}} = \bar{\boldsymbol{S}} \cdot \tilde{\boldsymbol{D}} + \overline{\boldsymbol{S}' \cdot \boldsymbol{D}'} = \bar{\boldsymbol{S}} \cdot (\overline{\tilde{\boldsymbol{D}} + \tilde{\boldsymbol{D}}''})$$

$$+ \overline{\boldsymbol{S}' \cdot \boldsymbol{D}'} = \bar{\boldsymbol{S}} \cdot \tilde{\boldsymbol{D}} + \bar{\boldsymbol{S}} \cdot \overline{\boldsymbol{D}''} + \overline{\boldsymbol{S}' \cdot \boldsymbol{D}'} \tag{8}$$

$$\bar{\dot{p}} = \overline{\partial_t(p) + \dot{\boldsymbol{x}} \cdot \text{grad}\,p} = \partial_t(\bar{p})$$

$$+ \tilde{\dot{\boldsymbol{x}}} \cdot \text{grad}\,\bar{p} + \overline{\dot{\boldsymbol{x}}''} \cdot \text{grad}\,\bar{p} + \overline{\dot{\boldsymbol{x}}' \cdot \text{grad}\,p'}$$

in which $\overline{\dot{\boldsymbol{x}}''} = -\overline{(\rho\dot{\boldsymbol{x}})}/\bar{\rho}$ is the turbulent mass flux, which can be derived from Eq. (4), $\dot{\boldsymbol{x}}' \cdot \text{grad}\,p'$ is the pressure gradient-velocity correlation and, finally, the turbulent dissipation rate $\varepsilon = \overline{\boldsymbol{S}' \cdot \boldsymbol{D}'}$. Often the pressure gradient-velocity correlation is decomposed into the pressure-dilatation correlation $\overline{p'\text{div}\dot{\boldsymbol{x}}'}$, and the pressure-velocity gradient correlation $\text{div}(\overline{p'\dot{\boldsymbol{x}}'})$. Hence, in order to achieve closure, we need models for the following turbulence correlations: 1) the density weighted Reynolds stress $\boldsymbol{R}$, 2) the density weighted Reynolds flux $\boldsymbol{r}$, 3) the turbulent mass flux $\overline{\dot{\boldsymbol{x}}''}$, 4) the turbulent dissipation rate ε, and 5) the pressure gradient-velocity correlation $\overline{\dot{\boldsymbol{x}}' \cdot \text{grad}\,p'}$.

The problem of calculating the unknown turbulence correlations can be approached on varying levels of complexity. For the density weighted Reynolds stress $\boldsymbol{R}$ the most popular approach is based on the eddy-viscosity concept of Boussinesq[15] relating $\boldsymbol{R}$ to the rate of strain tensor $\tilde{\boldsymbol{D}}$ according to $\boldsymbol{R} = 2/3\bar{\rho}k\boldsymbol{I} + 2\mu_T\tilde{\boldsymbol{D}}_D$, where μ_T is the eddy viscosity and $\tilde{\boldsymbol{D}}_D$ is the deviatoric part of $\tilde{\boldsymbol{D}}$. The eddy viscosity is then provided by an algebraic expression, in the k–ε model it is generally assumed that $\mu_T = C_\mu\bar{\rho}k^2/\varepsilon$, where $C_\mu = 0.09$ is a dimensionless model constant. The turbulent kinetic energy k and the turbulent dissipation rate ε are calculated from modeled versions of their exact transport equations. In this paper we have adopted the k–ε model of Jones and Launder[16]:

$$\partial_t(\bar{\rho}k) + \text{div}(\bar{\rho}k\tilde{\dot{\boldsymbol{x}}}) = -\tilde{\boldsymbol{D}} \cdot \boldsymbol{R} + \text{div}[(\mu_T/\sigma_k)\text{grad}\,k] - \bar{\rho}\varepsilon \tag{9a}$$

$$\partial_t(\bar{\rho}\varepsilon) + \text{div}(\bar{\rho}\varepsilon\tilde{\dot{\boldsymbol{x}}}) = -C_{\varepsilon 1}\bar{\rho}(\varepsilon/k)\tilde{\boldsymbol{D}} \cdot \boldsymbol{R}$$

$$+ \text{div}[(\mu_T/\sigma_\varepsilon)\text{grad}\,\varepsilon] - C_{\varepsilon 2}\bar{\rho}(\varepsilon^2/k) \tag{9b}$$

The right-hand side of Eq. (9), except for the term $-\tilde{\boldsymbol{D}} \cdot \boldsymbol{R}$ in Eq. (9a) representing production of turbulent kinetic energy, contains modeled higher order unknown correlations. These modeled correlations represent diffusion and dissipation of turbulent kinetic energy and pressure strain in Eq. (9a), and production, turbulent transport, and destruction of dissipation in Eq. (9b). The dimensionless model constants are given the values $\sigma_k = 1.00$, $\sigma_\varepsilon = 1.31$, $C_{\varepsilon 1} = 1.44$, and $C_{\varepsilon 2} = 1.92$. However, models based on the eddy-viscosity approach have significant deficiencies, such as the inability to properly account for streamline curvature, rotational strains, and other body force effects, as well as negligence of nonlocal and history effects. For further information see Ref. 7.

To circumvent these deficiencies second-order closure models or DRSM aiming at solving a modeled transport equation for the Reynolds stress have been developed. Today several different models have been suggested; most of them share the feature that a separate modeled transport equation for the dissipation rate has to be solved along with the transport equation for the Reynolds stress. We have adopted the DRSM of Gibson and Younis[18]:

$$\partial_t(\boldsymbol{R}) + \mathrm{div}(\boldsymbol{R} \otimes \tilde{\boldsymbol{x}}) = \boldsymbol{P} + \mathrm{div}[C_s(k/\varepsilon)(\mathrm{grad}\,\boldsymbol{R})\boldsymbol{R}] - C_1\boldsymbol{R}_D - C_2\boldsymbol{P}_D + \tfrac{2}{3} - \bar{\rho}\varepsilon\boldsymbol{I} \quad (10a)$$

$$\partial_t(\bar{\rho}\varepsilon) + \mathrm{div}(\bar{\rho}\varepsilon\tilde{\boldsymbol{x}}) = \mathrm{div}[C_d(\varepsilon/k)\boldsymbol{R}\,\mathrm{grad}\,\varepsilon] - C_{\varepsilon 1}\bar{\rho}(\varepsilon/k)\tilde{\boldsymbol{D}}\cdot\boldsymbol{R} - C_{\varepsilon 2}\bar{\rho}(\varepsilon^2/k) \quad (10b)$$

where the subscript D denotes the deviatoric part. The right-hand side of Eq. (10a), except for the term $\boldsymbol{P} = -(\boldsymbol{R}\tilde{\boldsymbol{L}}^T + \tilde{\boldsymbol{L}}\boldsymbol{R}^T)$ representing production of Reynolds stress, contains modeled higher order unknown correlations. In Eq. (10a) these modeled correlations represent diffusion, pressure strain, and dissipation of Reynolds stress; in Eq. (10b) they represent production, turbulent transport, and destruction of dissipation. The dimensionless model constants are assigned the values $C_s = 0.11$, $C_1 = 1.80$, $C_2 = 0.60$, $C_d = 0.16$, $C_{\varepsilon 1} = 1.44$, and $C_{\varepsilon 2} = 1.92$.

For the density weighted Reynolds flux $\boldsymbol{r}$ and for the turbulent mass flux $\overline{\dot{\boldsymbol{x}}''}$, the most popular approaches are based on gradient transport models; here we have adopted the models suggested by Cebeci and Smith[19]:

$$\boldsymbol{r} \approx -(C_\mu/\sigma_T)\bar{\rho}(k^2/\varepsilon)\mathrm{grad}\,\tilde{h}$$
$$\overline{\dot{\boldsymbol{x}}''} \approx (C_\mu k^2)/(\bar{\rho}\sigma_p\varepsilon)\mathrm{grad}\,\bar{\rho} \quad (11)$$

where $\sigma_T \approx 0.7$ and $\sigma_p = 1.1$. Finally, the pressure gradient-velocity correlation can be decomposed as $\overline{\dot{\boldsymbol{x}}'\cdot\mathrm{grad}\,p'} = \mathrm{div}(\overline{p'\dot{\boldsymbol{x}}'}) - \overline{p'\mathrm{div}\dot{\boldsymbol{x}}'}$, in which the first term normally is neglected; we will follow Speziale and Sarkar[17] and neglect the pressure-dilatation correlation as well.

Large-Eddy Simulation Model

In LES it is assumed that the flow can be decomposed into two parts. The first part contains the large-scale components, which depend on the boundary conditions and the geometry, whereas the second part contains the subgrid-scale components whose effects on the large scales must be modeled. The large-scale components driving the flow are assumed to contain a significant part of the turbulent energy which means that the cutoff wave number must be sufficiently high. However, using SGS models, we can truncate the representation at scales considerably larger than the Kolmogorov scale. To obtain the governing equations of the large-scale motion, spatial filtering is adopted. The idea of applying an averaging operator to the fluid dynamic equations, with averaging typically over the grid volume to filter out the SGS motions, has been known since the early work of Reynolds.[20] Explicit calculations are then made for the filtered variables or large-scale components after assumptions are made for the SGS stresses and fluxes that arise from the filtering process. Only the SGS motions, relative to the computational grid spacings, need modeling. This is in sharp contrast to RAS in which all of the deviations from the average fields are modeled.

More precisely, any flow variable ϕ can be decomposed into large-scale and SGS components and filtered by a convolution integral according to

$$\phi = \bar{\phi} + \phi', \qquad \bar{\phi} = \int_D G(\boldsymbol{x}-\boldsymbol{z},\Delta)\phi(\boldsymbol{x},t)\,\mathrm{d}^3\boldsymbol{z} \quad (12a)$$

$$\phi = \bar{\phi} + \phi''$$

$$\overline{\rho\phi} = \bar{\rho}\bar{\phi} = \int_D G(\boldsymbol{x}-\boldsymbol{z},\Delta)\rho(\boldsymbol{x},t)\phi(\boldsymbol{x},t)\,\mathrm{d}^3\boldsymbol{z} \quad (12b)$$

where the kernel $G(\boldsymbol{x}-\boldsymbol{z},\Delta)$ is the filter function with a characteristic width Δ, and the integration is over the entire computational domain D. Applying the filter G to the variable ϕ means that the amplitudes of the low wave number spatial Fourier components are reduced. The filter function must be normalized according to

$$\int_D G(\boldsymbol{x}-\boldsymbol{z},\Delta)\,\mathrm{d}^3\boldsymbol{z} = 1$$

In the limit as the mesh size goes to zero, Eq. (12a) becomes

$$\lim_{\Delta\to 0}\int_D G(\boldsymbol{x}-\boldsymbol{z},\Delta)\phi(\boldsymbol{z},t)\,\mathrm{d}^3\boldsymbol{z} = \phi(\boldsymbol{x},t)$$

Finally, the filter function should be taken to be an infinitely differentiable function of bounded support in a bounded region, more precisely, $G = G(\boldsymbol{x}-\boldsymbol{z},\Delta) \in D$, in which $D = \{\psi \in C^n(R^3)\}$ and ψ has compact support.

The governing equations for the large-scale components are obtained by filtering Eq. (3) with the convolution integral (12), hence,

$$\partial_t(\bar{\rho}) + \mathrm{div}(\bar{\rho}\tilde{\boldsymbol{x}}) = 0$$

$$\partial_t(\bar{\rho}\tilde{\boldsymbol{x}}) + \mathrm{div}(\bar{\rho}\tilde{\boldsymbol{x}}\otimes\tilde{\boldsymbol{x}}) = -\mathrm{grad}\,\bar{p} + \mathrm{div}(\bar{\boldsymbol{S}} - \boldsymbol{B}) + \bar{\rho}\tilde{\boldsymbol{b}} \quad (13)$$

$$\partial_t(\bar{\rho}\tilde{h}) + \mathrm{div}(\bar{\rho}\tilde{h}\tilde{\boldsymbol{x}}) = \bar{\dot{p}} + \overline{\boldsymbol{S}\cdot\boldsymbol{D}} + \mathrm{div}(\bar{\boldsymbol{h}} - \boldsymbol{b}) + \bar{\rho}\bar{\sigma}$$

where the filtered thermodynamic pressure is given by $\bar{p} = \bar{\rho}R\tilde{\theta}$ and where we have introduced the density weighted SGS Leonard, cross, and Reynolds quantities $\{\boldsymbol{L},\boldsymbol{l}\}$, $\{\boldsymbol{C},\boldsymbol{c}\}$, and $\{\boldsymbol{R},\boldsymbol{r}\}$ by

$$\boldsymbol{B} = \bar{\rho}(\widetilde{\tilde{\boldsymbol{x}}\otimes\tilde{\boldsymbol{x}}} - \tilde{\boldsymbol{x}}\otimes\tilde{\boldsymbol{x}}) = \bar{\rho}(\widetilde{\tilde{\tilde{\boldsymbol{x}}}\otimes\tilde{\boldsymbol{x}}} - \tilde{\boldsymbol{x}}\otimes\tilde{\boldsymbol{x}}) + \bar{\rho}(\widetilde{\tilde{\tilde{\boldsymbol{x}}}\otimes\dot{\boldsymbol{x}}''} + \widetilde{\dot{\boldsymbol{x}}''\otimes\tilde{\boldsymbol{x}}}) + \bar{\rho}(\widetilde{\dot{\boldsymbol{x}}''\otimes\dot{\boldsymbol{x}}''}) = \boldsymbol{L}+\boldsymbol{C}+\boldsymbol{R}$$

$$\boldsymbol{b} = \bar{\rho}(\widetilde{\tilde{\boldsymbol{x}}h} - \tilde{\tilde{\boldsymbol{x}}}\tilde{h}) = \bar{\rho}(\widetilde{\tilde{\boldsymbol{x}}\tilde{h}} - \tilde{\tilde{\boldsymbol{x}}}\tilde{h}) + \bar{\rho}(\widetilde{\tilde{\boldsymbol{x}}h''} + \widetilde{\dot{\boldsymbol{x}}''\tilde{h}} + \bar{\rho}(\widetilde{h''\dot{\boldsymbol{x}}''}) = \boldsymbol{l}+\boldsymbol{c}+\boldsymbol{r} \quad (14)$$

Assuming that SGS fluctuations in the thermal conductivity and in the viscosities can be neglected in the flow except for a thin sublayer near the wall results in the following approximate expressions for the heat conduction vector and the viscous stress tensor:

$$\bar{\boldsymbol{h}} = \overline{\kappa\,\mathrm{grad}\,\theta} \approx \bar{\kappa}\,\mathrm{grad}\,\tilde{\theta} = (\bar{\kappa}/\bar{C}_p)\mathrm{grad}\,\tilde{h}$$

$$\bar{\boldsymbol{S}} = \overline{\lambda\,\mathrm{tr}\,(\boldsymbol{D})\boldsymbol{I} + 2\mu\boldsymbol{D}} \approx \bar{\lambda}\,\mathrm{tr}\,(\tilde{\boldsymbol{D}})\boldsymbol{I} + 2\bar{\mu}\tilde{\boldsymbol{D}} \quad (15)$$

where $\bar{\kappa} = \kappa(\bar{\rho},\tilde{\theta})$, $\bar{C}_p = C_p(\tilde{\theta})$, $\bar{\mu} = \mu(\bar{\rho},\tilde{\theta})$, and $\bar{\lambda} = \lambda(\bar{\rho},\tilde{\theta})$. The dissipation function and the substantial time derivative of pressure can, with the aid of Eq. (15), be calculated according to

$$\overline{\boldsymbol{S}\cdot\boldsymbol{D}} = \overline{(\tilde{\boldsymbol{S}}+\boldsymbol{S}')\cdot(\tilde{\boldsymbol{D}}+\boldsymbol{D}'')} = \overline{\tilde{\boldsymbol{S}}\cdot\tilde{\boldsymbol{D}}} + \overline{\tilde{\boldsymbol{S}}\cdot\boldsymbol{D}''} + \overline{\boldsymbol{S}'\cdot\tilde{\boldsymbol{D}}} + \overline{\boldsymbol{S}'\cdot\boldsymbol{D}''}$$

$$\bar{\dot{p}} = \overline{\partial_t(p) + \dot{\boldsymbol{x}}\cdot\mathrm{grad}\,p} = \partial_t(\bar{p}) + \overline{\tilde{\dot{\boldsymbol{x}}}\cdot\mathrm{grad}\,\bar{p}} + \overline{\tilde{\dot{\boldsymbol{x}}}\cdot\mathrm{grad}\,p'} + \overline{\dot{\boldsymbol{x}}''\cdot\mathrm{grad}\,\bar{p}} + \overline{\dot{\boldsymbol{x}}'\cdot\mathrm{grad}\,p'} \quad (16)$$

Both contain three additional terms that have to be prescribed before closure is accomplished; for comparison with RAS, see Eq. (8). An alternative decomposition to Eq. (16) has been discussed by Erlebacher et al.[7] For this initial study we choose to neglect the higher order correlations in Eq. (16), since their effects are expected to be small, and calculate the dissipation function and the substantial time derivative of pressure according to $\overline{\boldsymbol{S}\cdot\boldsymbol{D}} = \tilde{\boldsymbol{S}}\cdot\tilde{\boldsymbol{D}}$ and $\bar{\dot{p}} = \partial_t(\bar{p}) + \tilde{\dot{\boldsymbol{x}}}\cdot\mathrm{grad}\,\bar{p}$.

The quantities appearing in the filtered set of balance equations (13) can be divided into four categories: 1) $\bar{\rho}, \tilde{\boldsymbol{x}}, h$, 2) $\boldsymbol{R}, \boldsymbol{r}$, 3) $\boldsymbol{L}, \boldsymbol{l}, \boldsymbol{C}, \boldsymbol{c}$, and 4) $\tilde{\boldsymbol{b}}, \bar{\sigma}, \bar{p}, \overline{\boldsymbol{S}\cdot\boldsymbol{D}}$. The quantities in group 1 represent the large-scale component of the variables, and the time and space evolution of these is the objective of LES. The quantities in group 2 represent the correlations of SGS fluctuations and require modeling; their major effect is dissipation or outscatter. The quantities in group 3 are particular only to LES and do not appear in RAS. The Leonard quantities mainly give rise to redistribution among the

various large scales, whereas the major effect of the cross quantities seems to be backscatter, i.e., transfer from small scales back to larger scales. The Leonard quantities can be calculated exactly although the cross quantities must be modeled. Models for the cross quantities can be developed separately and used together with models for the Reynolds quantities and the expressions for the Leonard quantities. Sometimes the effects of Leonard and cross quantities are neglected, and occasionally the cross quantities are lumped into group 2. The quantities in group 4 represent source terms and nonlinear terms from the energy equation. If these terms are nonlinear, they cannot be evaluated by straightforward methods due to the filtering process, e.g., see Ref. 7.

The basic idea of SGS modeling is to represent phenomenologically the macroscopic effects of fluid flow occurring on the space scales not resolved. This commonly means representing physical actions at length scales which are smaller than a computational cell. These SGS models must mimic the actual physical processes of dissipating turbulent energy at SGS:s to heat. On the average, kinetic energy is transferred from the large eddies to the small ones; there is energy flow in both directions, but the net flow is usually toward the small scales. Leslie and Quarini[21] estimated that the gross transfer to the small scales is about 1.5 times the net transfer. The SGS terms in Eq. (13) must represent the effects of these transfers on the large scales. In the normal situation, the net energy transfer to the small eddies appears to be dissipation from the large eddies, energy is lost and will not reappear.

There are many different ways of postulating or deriving SGS models in LES since several quantities or combinations of quantities are subject to modeling. Observe that SGS models only aim at describing the effects of the small-scale motions on the large-scale motions and can, thus, be of more universal character than traditional turbulence modeling. In this investigation we will not exploit the possibility of deriving alternative SGS models, which in principle can be done systematically within the frame of modern continuum physics making use of frame indifference and isotropic functions, but we will merely adopt one well-known SGS model.

Since the major effect of the Reynolds quantities is assumed to be dissipative, we should look for something like an eddy-viscosity model. For anisochoric flows the realizability criterion must be satisfied; this is automatically satisfied in isochoric flows since $\mathrm{tr}\,\tilde{\boldsymbol{D}} = \mathrm{div}\,\tilde{\boldsymbol{x}} = 0$. This naturally implies that this model should be of the generalized form $\boldsymbol{R} = \frac{2}{3}\bar{\rho}q_{sgs}\boldsymbol{I} + 2\mu_{sgs}\tilde{\boldsymbol{D}}_D$ where q_{sgs} is the kinetic energy of the SGS motions, μ_{sgs} denotes the SGS eddy viscosity, and $\tilde{\boldsymbol{D}}_D$ is the deviator of the rate of strain tensor. To close this relation we need to prescribe q_{sgs} and μ_{sgs}. Two approaches can be imagined. 1) Calculate both μ_{sgs} and q_{sgs} from algebraic expressions that have to be prescribed. 2) Postulate a transport equation for q_{sgs} and calculate μ_{sgs} from q_{sgs} and the SGS length $\lambda_{sgs} = \sqrt{c_D}\Delta$, where c_D is a dimensionless model coefficient. For practical reasons the first method is predominant, and this is also the method chosen here. Assuming that production of q_{sgs} equals dissipation of q_{sgs} we can, from the transport equation for q_{sgs}, derive a anisochoric version of the Smagorinsky model.[22] Adopting a similar approach for the SGS fluxes we find

$$\boldsymbol{R} \approx \tfrac{2}{3}c_I\bar{\rho}\Delta^2\|\tilde{\boldsymbol{D}}\|^2\boldsymbol{I} - 2c_D\bar{\rho}\Delta^2\|\tilde{\boldsymbol{D}}\|\tilde{\boldsymbol{D}}_D \tag{17a}$$

$$\boldsymbol{r} \approx -2c_H\bar{\rho}\Delta^2\|\tilde{\boldsymbol{D}}\|\mathrm{grad}\,\tilde{h} \tag{17b}$$

where $c_I = 0.0066$, $c_D = 0.0120$, and c_H are model constants,[7] and $\|\tilde{\boldsymbol{D}}\|$ is the Frobenius norm of the rate of strain tensor. It is customary to put $c_H = c_D/Pr_T$, where the turbulent Prandtl number $Pr_T \approx 0.7$.

SGS eddy-viscosity models of this type are found to do well in some homogeneous isochoric flows where there is no mean strain. In homogeneous isochoric flows with strain or shear, McMillan and Ferziger[23] have observed that the energy transfer can be reversed and transferred from the small scales to the large ones. Further, eddy-viscosity models seem not to do well in transitional flows since the small scales are not in equilibrium and the production equals dissipation argument is incorrect. Additionally, according to an analysis by Speziale et al.[5] the first term in the closure model (17a) does not correlate well with the results of DNS of nonreacting anisochoric turbulent flow.

The first attempts for improving the SGS modeling did not take the neglected Leonard and cross quantities into consideration but concentrated on trying to improve the SGS eddy-viscosity/diffusivity models by making analogies to the attempts made in RAS. Schumann[24] tried to solve a modeled version of a transport equation for q_{sgs} whereas Deardorff[25] tried to solve a modeled transport equation for the SGS Reynolds stress tensor. A more amemnable approach would be to include the Leonard and cross quantities in the SGS model. To model the effects of these, it can be assumed that the interaction between the large- and small-scale components of the flowfield takes place mainly between the segments of each field that are most like one another. The major interactions are, thus, between the smallest scales of the large-scale field and the largest scales of the small-scale fields. Since the interacting components are very much alike, it seems natural to have the model reflecting this. Hence, we must find some way of defining the small-scale component of the large-scale field. One way was suggested by Bardina et al.[26] Since filtering the large-scale component of a field produces a field whose content is still richer in the largest scales, this suggests models of the "scale similarity" type,

$$\begin{aligned}\boldsymbol{C} &\approx c_{B1}\bar{\rho}(\tilde{\tilde{\boldsymbol{x}}}\otimes\tilde{\tilde{\boldsymbol{x}}} - \tilde{\tilde{\boldsymbol{x}}}\otimes\tilde{\tilde{\boldsymbol{x}}})\\ \boldsymbol{c} &\approx c_{B2}\bar{\rho}(\tilde{\tilde{h}}\tilde{\tilde{\boldsymbol{x}}} - \tilde{\tilde{h}}\tilde{\tilde{\boldsymbol{x}}})\end{aligned} \tag{18}$$

Bardina arrived at a value of $c_{B1} = 1.1$ by correlating with data obtained from DNS of homogeneous isochoric nonreacting turbulent flow. However, in order to ensure that the transformation properties of $\boldsymbol{C}$ and $\boldsymbol{c}$ are the same when changing frame of reference, c_{B1} and c_{B2} must both equal unity.

What remains to be specified is a relation between the filter width Δ and the local geometry on the grid. For a nonuniform grid, it is not obvious how to determine the resolved length scale. Several measures have been proposed, see Deardorff[2] and Moin and Kim.[27] Here we have used

$$\Delta = \sqrt{\sum_{i=1}^{N}(\Delta x_i)^2} \tag{19}$$

where N is the number of spatial dimensions of the calculation domain. The choise of the filter width is important since it will determine the magnitude of the SGS quantities.

Methods for Discretizing the Governing Equations

The governing equations are discretized on a staggered mesh by a finite volume technique. This resolves many of the difficulties associated with the nonlinearities embedded in the fluid dynamics equations. In the LES model presented, the SGS terms explicitly provided are proportional to Δ^2 and, thus, the numerical scheme adopted must be of at least third-order accuracy to avoid implicit coupling between the SGS terms and the truncation error. For evaluating the convective fluxes we have made use of the monotonic third-order accurate scheme SMART of Gaskell and Lau.[28] The SMART scheme is based on an approach called curvature compensated convective transport (CCCT) and it strictly preserves the monotonicity of the solution by the inclusion of a flux limiter on the third-order accurate upwind-biased interpolation approximation. The flux limiter is closely related to the curvature terms. For the diffusive fluxes a third-order accurate difference interpolation approximation has been adopted. The time advance was made with a second-order accurate implicit Crank–Nicholson method. The discretized equations lead to a system in which all of the dependent variables are coupled together. The SIMPLER scheme[29] is used for "decoupling" velocity and pressure. Since we use the mass flux conserving transformation, the coupling between density and velocity is only through source terms. The energy equation and other transport equations are updated after updating the velocity and pressure.

The accuracy of the numerical scheme employed is of particular importance in LES since the truncation errors can introduce damping of the motion. If no SGS models are introduced (quasi-LES), a

certain amount of damping is wanted and necessary since no model is introduced for the damping effect of the unresolved SGS motion. However, in other calculations which simulate the damping effect of the turbulent motion through a special model, the numerical damping is undesired. Preliminary results obtained with a fourth-order accurate scheme which is under development are encouraging and indicate that the third-order scheme used here is sufficient.

Simulation Object and Related Initial and Boundary Conditions

To evaluate the predictive capabilities of the LES model we have conducted numerical simulations on a configuration corresponding to a flexible modular combustor with optical access, "validation rig" described in Ref. 8, on which a number of experimental measurements have been made, e.g., laser Doppler velocimetry (LDV) measurements of the velocity field. The rig consists of a rectilinear channel, with rectangular cross section, divided into an inlet section and a combustor section with a triangular shaped bluff body, see Fig. 1. The fluid was air, and the pressure at room temperature was atmospheric. The Re number, based on the bluff body height and the inlet velocity, was between 10^3 and 10^5 and the Ma number, based on the inlet velocity, was between 0.01 and 0.20.

All simulations started from complete rest, and the unsteady flow characteristics evolved naturally. At the inlet boundary, Dirichlet conditions for the velocity, pressure, and enthalpy were adopted. The velocity profiles used in the simulations were obtained from experimental LDV measurements revealing an almost plug shaped profile, whereas the pressure and enthalpy were given uniform values accross the inlet boundary. In RAS no artificial inlet disturbances were introduced whereas in some of the LES a white noise with an amplitude of 5% of the inlet velocity was added to the original velocity profile. At the outflow boundary, we have followed the recommendations of Gustavsson and Sundström[30] and applied boundary conditions for all but one dependent variable. Boundary conditions for the velocity components and the enthalpy are thus specified as zero Neumann conditions. In the RAS the wall boundary conditions were treated with logarithmic wall functions, see Refs. 16 and 18, respectively; in the LES, we followed the recommendation of Piomelli et al.[31] and used a relation between the wall shear stress and the velocity at the first grid point.

The computational grid used in all simulations was concentrated around the bluff body and near the channel walls and geometrically stretched in the other regions. The number of control volumes were 180×150 for the simulations done with the k–ε model and the DRSM, 400×60 for the two-dimensional LES, and $400 \times 60 \times 60$ for the three-dimensional LES. Grid refinement, made on the simulations using the k–ε model, showed that the results were grid independent, whereas grid refinement made on the simulations using two-dimensional LES showed that the spatial resolution was adequate; using more control volumes showed improvement, but the difference was insignificant. For the two-dimensional simulations powerful workstations (HP9000) were used whereas the three-dimensional simulations were performed on a Cray Y-MP/464, a speed of 215 Mflops was achieved.

Simulation Results and Comparison with Physical Experiments

The flow under consideration is a wall bounded wake flow. A wake can be characterized as a flow with a defect in the otherwise uniform stream and has decreasing velocity gradients with downstream distance. In this case the wake forms by separation of boundary layers and widening of the velocity profile. In this paper we will focus on presenting results from a case characterized by the inlet velocity, $w_0 = 17.3$ m/s, and the corresponding turbulence level, which was measured to 4%; for more details see Ref. 8. Experimentally measured data for the ensemble averaged velocity components, the rms-velocity components, and the turbulent shear stress are available at three cross sections, $z = 0.348$, $z = 0.460$ and also $z = 0.686$ downstream of the bluff body, as well as at the centerline $y = 0.060$, all experimental measurements are made at the plane $x = 0.12$.

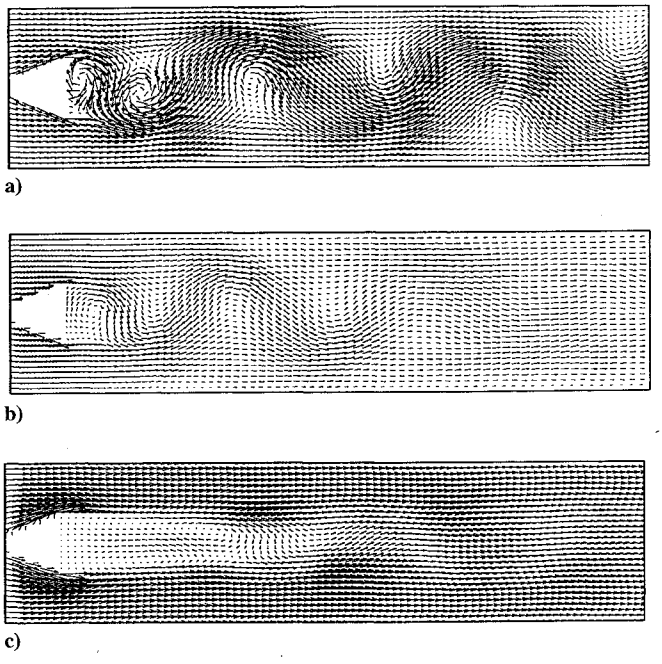

Fig. 2 Photographs of velocity vectors: a) velocity field as simulated by two-dimensional LES, 60×400 nodes, b) velocity field as simulated with three-dimensional LES, $60 \times 60 \times 400$ nodes, centerplane $x = 0.12$, and c) velocity field as simulated with two-dimensional k–ε model, 180×150 nodes.

Figure 2 shows a photograph of the velocity field when the flow is fully developed as simulated with two-dimensional LES (Fig. 2a), three-dimensional LES (Fig. 2b), and the k–ε model (Fig. 2c). From the results of the simulations we find that a short time period, about 0.1 s, is required for the initial conditions to develop into a physically realistic flow. During this period there is relatively little broadening of the wake, and the vorticity seems to concentrate. The unsteady behavior is due to vortex shedding, with vorticies alternatively shedding from the upper and lower edges of the bluff body, forming a von Kármán vortex street behind the bluff body with a well-defined shedding frequency. The strong vortex street is highly regular and persists very far downstream in the two-dimensional LES whereas in the three-dimensional LES the vortex street declines gradually. As we see from Figs. 2a and 2b, moving recirculation zones can appear between the wake and the walls, this is a phenomenon that previously has been observed experimentally for flows around circular cylinders at high Re numbers.[9] The appearence of such structures is the result of intermittent separations due to increased wall shear stress significantly influenced by the wall boundary conditions.[31] In Fig. 2 we can further observe the important structural differences between the two-dimensional and the three-dimensional LES. It was found from the simulations that the k–ε model had severe problems in developing the vortex shedding behavior unless the eddy viscosity was decreased to approximately 50% of what is prescribed originally; this effect was also presented by Franke and Rodi.[10] The DRSM used did not, in contradiction to what was anticipated, show any improved behavior over the k–ε model regarding the strength of the vortex shedding.

The Strouhal number $S^r = f\lambda_0/w_0$, based on the height of the bluff body λ_0 and the inlet velocity w_0 where f is the shedding frequency, was experimentally found to be $S^r = 0.24$, corresponding to 102 Hz (Ref. 8). From the RAS the Strouhal number was found to be $S = 0.18$ for the k–ε model and $S^r = 0.20$ for the DRSM. For the two-dimensional LES the Strouhal number was found to be $S^r = 0.25$ and for the three-dimensional LES it was found to be $S^r = 0.24$. Hence, both the two-dimensional and the three-dimensional LES were able to capture the correct frequency of the established vortex street. After the transient state gradually has grown into a physically realistic state, the velocity and pressure time series are highly periodic both on the centerline and in the shear layers at different locations downstream of the bluff body in both the two-dimensional and three-dimensional LES.

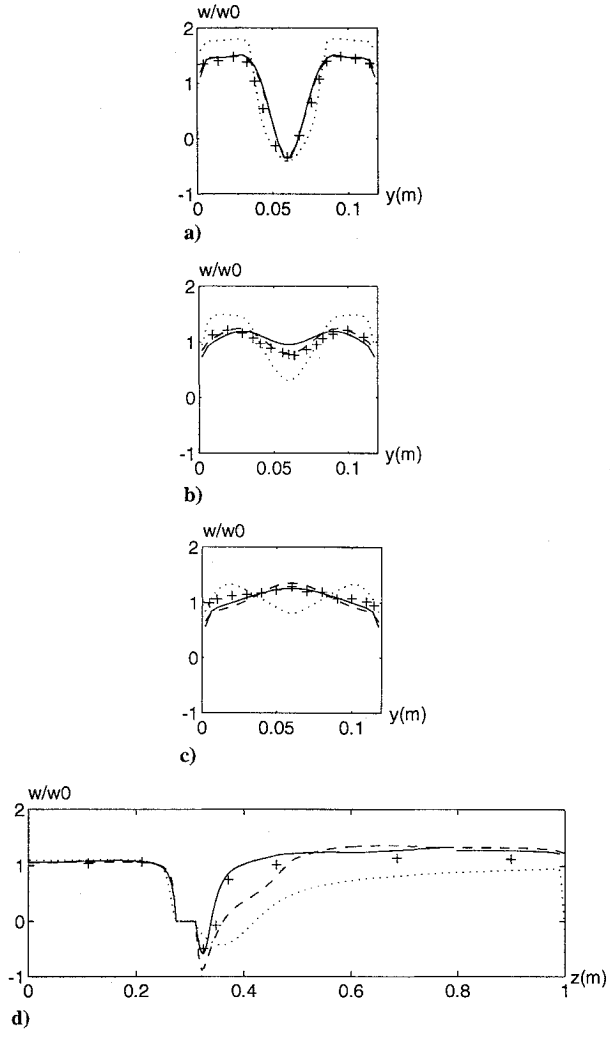

Fig. 3 Normalized ensemble averaged streamwise velocity component, inlet velocity at the centerline w_0; + indicates measurements, solid lines three-dimensional LES, dashed lines two-dimensional LES, and dotted lines k–ε model: a) $z = 0.348$, b) $z = 0.460$, c) $z = 0.686$, and d) plane $y = 0.060$.

In Fig. 3 the ensemble averaged streamwise velocity component at the three cross sections downstream of the bluff body and at the centerline is presented. The ensemble averaged value of any field ϕ is calculated by the expectation value operator $\langle\cdot\rangle$ defined by $\langle\phi\rangle = (\sum_\alpha \phi^\alpha)/N$, where α is the realization number and N the total number of realizations, here $N = 5000$. By comparison of the streamwise velocity profiles (Figs. 3a–3c) it is observed that both the two-dimensional and, in particular, the three-dimensional LES correlates well with physical experiments whereas the k–ε model give less accurate profiles. Farther downstream (Fig. 3c), the two-dimensional LES somewhat overpredicts the streamwise velocity component at the core compared to the measurements. The reason for this overprediction is that the vortex street persists very far downstream in the two-dimensional LES whereas in the three-dimensional LES the vortex street declines gradually. A physical explanation for this structural difference between the two-dimensional and the three-dimensional LES is believed to be the lack of realistic turbulence production mechanisms, such as vortex stretching, in the two-dimensional LES. Comparing the streamwise velocity profiles at the centerline we note that in front of the bluff body the results are not much influenced by the simulation method used and the numerical and physical experiments correlate well. In the wake region, differences due to simulation method used are observed. The k–ε model overpredicts the length of the separation zone considerably and also fails to reproduce the correct magnitude of the streamwise velocity component behind the bluff body. The two-dimensional LES overpredicts the length of the separation region to a small extent, and the agreement with the data is not satisfactory;

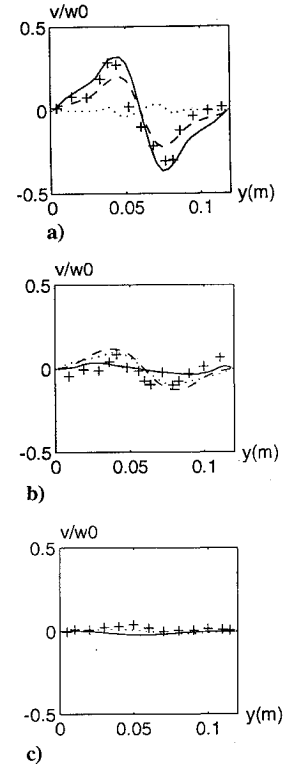

Fig. 4 Normalized ensemble averaged lateral velocity component, inlet velocity at the centerline w_0; + indicates measurements, solid lines three-dimensional LES, dashed lines two-dimensional LES, and dotted lines the k–ε model: a) z = 0.348, b) z = 0.460, and c) $z = 0.686$.

the magnitude of the streamwise velocity component is overpredicted close to the bluff body, and the shape of the velocity profile is not reproduced correctly. The three-dimensional LES predicts the separation region and the downstream flow very well.

In Fig. 4 the ensemble averaged lateral velocity component at the three selected cross sections is presented. A comparison of the lateral velocity profiles clearly reveals that the k–ε model and the DRSM (not shown) do not produce enough momentum exchange in the lateral direction. In vortex-shedding flow the momentum exchange in the lateral direction is mainly due to the periodic fluctuations which, thus, are underpredicted by the k–ε model. As seen from Figs. 4a–4c the lateral velocity profiles obtained from the two-dimensional LES show good agreement with measurements in all three cross sections regarding both shape and magnitude. The profiles obtained from the three-dimensional LES also show good agreement with experimental data, except for Fig. 4b corresponding to the cross section at $z = 0.460$. This particular discrepancy may originate from lack of spatial resolution or locally high-geometrical stretching of the computational grid in the streamwise direction close to this cross section. The result can probably be improved by using either local grid refinement or multiblock techniques.

In Fig. 5 the rms-velocity fluctuation profiles, obtained from measurements and from two-dimensional and three-dimensional LES, at the three selected cross sections are presented. The rms-velocity fluctuations are local measures of the standard deviation of the velocity field and, thus, also measures of the strength of the turbulent fluctuations. The rms-velocity fluctuations are defined and calculated by $\dot{x}_{\text{rms}} = \sqrt{\langle \dot{x}'^2 \rangle}$ where the fluctuations are defined as $\dot{x}' = \tilde{\dot{x}} - \langle \tilde{\dot{x}} \rangle$. The general agreement between simulated rms-velocity profiles and measured profiles are good for both velocity components. However, the profiles from the two-dimensional simulations show a correct shape, but the magnitude is systematically overpredicted, especially for the lateral components where deviations of up to an order of magnitude is observed (Figs. 5b and 5c). For the three-dimensional LES we have better agreement between the simulated and measured profiles except for Fig. 5b, corresponding to the cross section at $z = 0.460$. This indicates the importance of three-dimensional effects not possible to include in two-dimensional

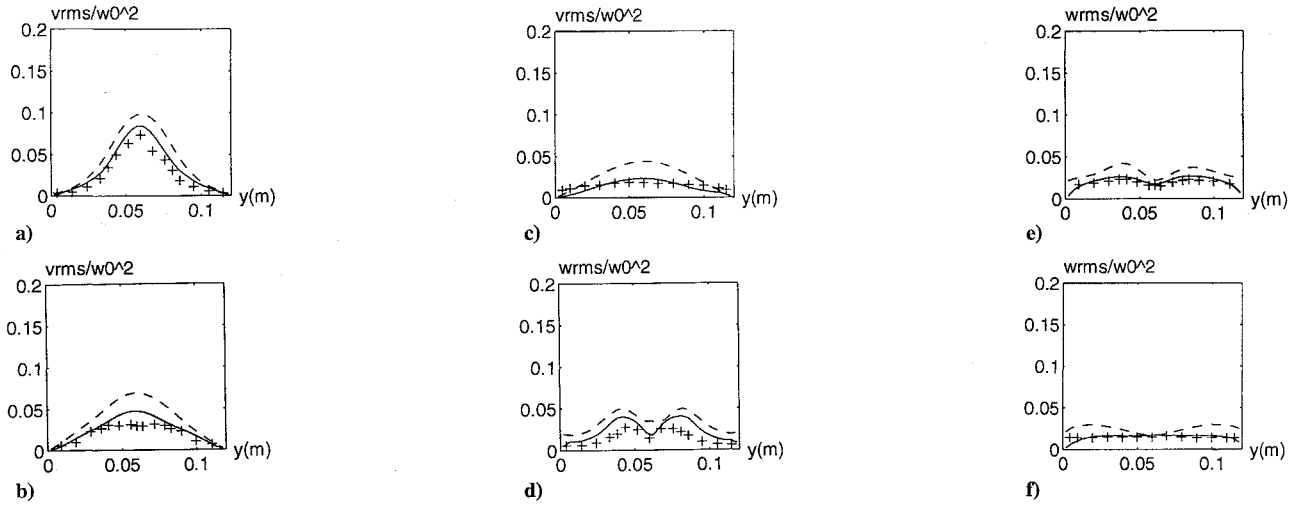

Fig. 5 Normalized rms-velocity components, inlet velocity at the centerline w_0; + indicates measurements, solid lines three-dimensional LESs, and dashed lines two-dimensional LESs: a) lateral component, $z = 0.348$, b) lateral component, $z = 0.460$, c) lateral component, $z = 0.686$, d) streamwise component, $z = 0.348$, e) streamwise component, $z = 0.460$, and f) lateral component, $z = 0.686$.

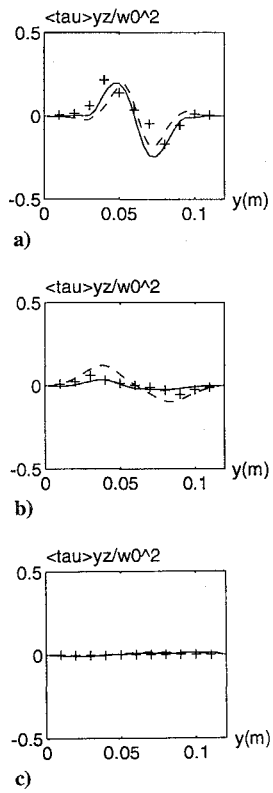

Fig. 6 Normalized ensemble averaged turbulent shear stress $\langle\tau\rangle_{yz}$, inlet velocity at the centerline w_0; + indicates measurements, solid lines three-dimensional LES, dashed lines two-dimensional LES; locations: a) $z = 0.348$, b) $z = 0.460$, and c) $z = 0.686$

LES. The discrepancy noted in the rms-velocity fluctuation profile at $z = 0.460$ is the direct consequence of the discrepancy observed in the lateral velocity profile at the same cross section.

The ensemble averaged turbulent shear stress in the yz plane, obtained from measurements and from two-dimensional simulations at the three selected cross sections is presented in Fig. 6. The ensemble averaged turbulent stresses are calculated according to their definition, i.e., $\langle\tau\rangle = \langle\bar{\rho}\rangle\langle\dot{x}' \otimes \dot{x}'\rangle$. From the LESs all other turbulent stress and flux components are also available, in fact, assuming negligible density fluctuations, the square root of the diagonal components of $\langle\tau\rangle$ are already presented and described in Fig. 5. Here, the agreement between simulated turbulent stress profiles and experimentally measured profiles are good both regarding the two-dimensional and, especially, the three-dimensional case. However, the two-dimensional LES slightly overpredicts the turbulent shear stresses at $z = 0.460$ (Fig. 6b) but, again, the shape of the profile is correct whereas the three-dimensional LES show overall good correlation with measurements.

Discussion and Interpretation of the Simulation Results

The results of the LES model described can now serve as foundation for a brief discussion concerning the mechanism of the large-scale structures characterizing the flowfield. In Fig. 7 some quantities are plotted at the center plane ($x = 0.120$) in a full height section of a 0.240 m length starting at $z = 0.330$. The quantities used to investigate the flow are the fluctuating velocity field ($\dot{x}' = \tilde{\dot{x}} - \langle\tilde{\dot{x}}\rangle$), the spanwise vorticity component ($\tilde{\omega}_x = 1/2\,\mathrm{curl}\,\tilde{\dot{x}} \cdot \boldsymbol{e}_x$ where $\boldsymbol{e}_x$ is the unit vector in the x direction), the kinetic energy of the fluctuating motion ($k = 1/2\dot{x}' \cdot \dot{x}'$), the production of kinetic energy due to the fluctuating motion [$p = -\tau \cdot \tilde{\boldsymbol{D}}$ where $\tau = \bar{\rho}(\dot{x}' \otimes \dot{x}')$ and $\tilde{\boldsymbol{D}} = 1/2(\mathrm{grad}\,\tilde{\dot{x}} + \mathrm{grad}\,\tilde{\dot{x}}^T)$], the rate of strain ($||\tilde{\boldsymbol{D}}||$), the normalized vortex stretching ($\zeta = \tilde{\omega} \cdot \tilde{\boldsymbol{L}}\tilde{\omega}/\tilde{\omega}^2$, where the vorticity vector is given by $\tilde{\omega} = 1/2\mathrm{curl}\,\tilde{\dot{x}}$), the dissipation of kinetic energy due to the fluctuating motion ($\varepsilon = \boldsymbol{S}' \cdot \boldsymbol{D}'$ where $\boldsymbol{S}' = \lambda\,\mathrm{div}\,\dot{x}' + 2\mu\boldsymbol{D}'$), and, finally, the dilatation ($\chi = \mathrm{div}\,\tilde{\dot{x}}$). Topologically, the flow structure can be characterized by extremum points (here denoted centers) and saddle points denoted by + and ×, respectively. The velocity vector field of Fig. 7a and the vorticity field of Fig. 7b both show well-organized vortical motion around the centers and also specify the saddle points. Since the fluid outside the large-scale structures forming the vortex street is engulfed into the wake region mostly downstream of the structure, the kinetic energy of the fluctuating motion at the front is lower than at the back, and according to Fig. 7c lower contour levels at the front extend toward the wake centerline ($y = 0.060$). This implies that a significant amount of fluid can be entrained from the opposite side of the wake across the centerline and also suggests that the vortex street is not a continuous sheet but perforated. Contours of production of kinetic energy due to the fluctuating motion (Fig. 7d) and rate of strain (Fig. 7e) are observed to have local maxima near the saddle points. The intense strain field in the saddle region appears to be the consequence of vortex stretching induced by successive like-signed vortices shown in Fig. 7f. Thus, significant production of large-scale turbulence due to large-scale structures occurs in the saddle regions. Dissipation of kinetic energy of the fluctuating motion, shown in Fig. 7g occurs in a highly localized fashion, predominantly at front of the large-scale structures where the kinetic energy of the fluctuating motion is lower. To investigate the influence of local compression and expansion effects present in the flow, the dilatation χ representing the relative change of volume per unit of time is shown in Fig. 7h. For a compressible

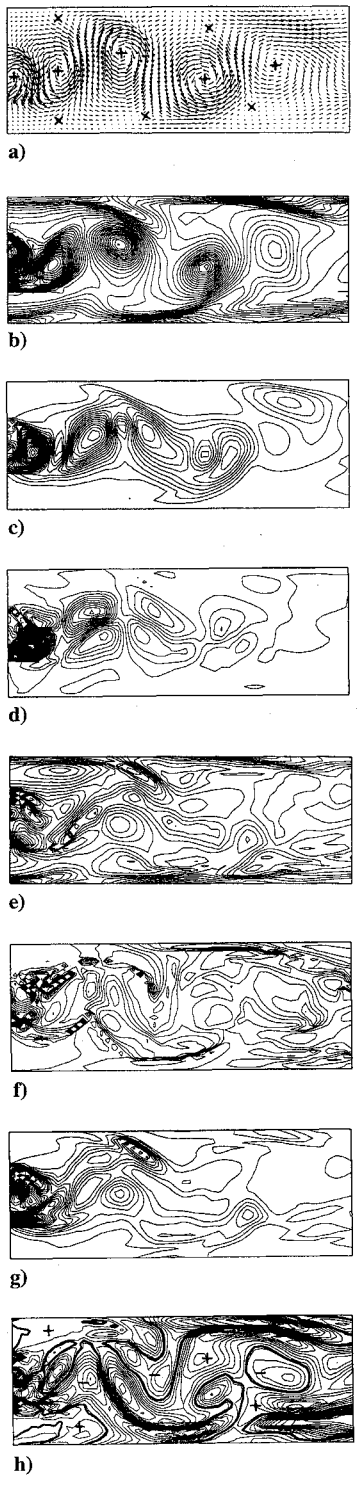

Fig. 7 Three-dimensional LES results at center plane $x = 0.120$ in full height section of 0.240 m length at $z = 0$: a) instantaneous fluctuating velocity field, b) contours of the spanwise vorticity, c) fluctuating kinetic energy, d) production of fluctuating kinetic energy, e) rate of strain, f) vortex stretching, g) dissipation of turbulent kinetic energy, and h) dilatation.

fluid χ can take all values in the range $-\infty < \chi < \infty$, whereas for an incompressible fluid, χ can only take the value zero, thus only admitting isochoric motion. In the case of a compressible fluid $\chi > 0$ corresponds to an expansion state, $\chi < 0$ corresponds to a compression state, and $\chi = 0$ corresponds to an isochoric state. By examining Fig. 7h we find connected areas of expansion (denoted by a + sign) and connected areas of compression (denoted by a − sign). Separating the regions of expansion and compression are thin sheets with $\chi = 0$ (denoted by a thick solid line). Regions with $\chi < 0$ are, in general, found outside the vortex street but also as isolated

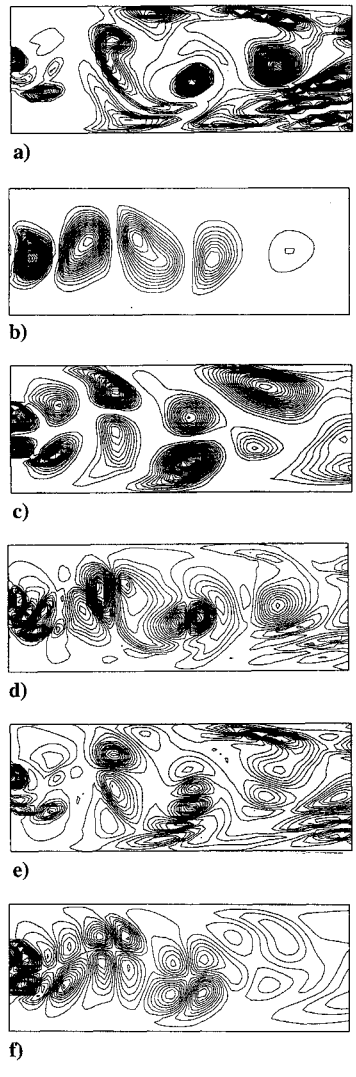

Fig. 8 Three-dimensional LES results at center plane $x = 0.120$ in full height section of 0.240 m length at 0.330; contours of the instantaneous turbulent stresses: a) normal stress component τ_{xx}, b) normal stress component τ_{yy}, c) normal stress component τ_{zz}, d) shear stress component τ_{xy}, e) shear stress component τ_{xz}, and f) shear stress component τ_{yz}.

spots within the vortex street farther downstream. Comparing the dilatation with the other quantities showed in Fig. 7 reveals that ζ and χ show common anatomy in regions of low-vortex stretching. From the decomposition of the vortex stretching in isotropic and deviatoric parts, $\zeta = \chi + (\tilde{\omega} \cdot \tilde{\boldsymbol{D}}_D \tilde{\omega})/\tilde{\omega}^2$, we observe that the dilatation affects the magnitude of the vortex stretching. Similarly, from the decomposition of the production of kinetic energy due to the fluctuating motion, $p = -(\frac{1}{3}\tilde{\rho} k \chi + \tau \cdot \tilde{\boldsymbol{D}}_D)$, we observe that the dilatation affects the production but obviously to a smaller extent.

From these results, the mechanism of the large-scale structure in unsteady wake flow emerges; the strong spanwise vorticity induces the large-scale motion of external fluid along the converging separatrix. The engulfed fluid is advected to the saddle region where most production of small-scale fluctuation takes place as a consequence of vortex stretching along the diverging separatrix. The fluctuations produced are continuously advected from this region into the structure and also away from the central portion of the wake.

In Fig. 8 the instantaneous turbulent stresses $\tau = \rho(\dot{x}' \otimes \dot{x}')$ representing transport of momentum at the center plane ($x = 0.120$) are shown. Comparing the contours of the instantaneous turbulent normal stress component τ_{xx} with the fluctuating velocity field of Fig. 7a we observe that the large-scale structures coincide with the extrema of τ_{xx} signifying momentum entrainment in the spanwise direction through to the large-scale structures. A proper SGS model for two-dimensional LES, however, should create the effect of this

entrainment mechanism, which is not the case here. The SGS model adopted is not strictly valid for two-dimensional simulations, so this remark should not be taken as an argument against its proper use in two-dimensional simulations. The fluctuating motion generates extrema in τ_{zz} above and below each vortex, with $\dot{x}_z$ positive for one extremum and negative for the other, see Fig. 8c. Similarly, the alternating extrema in τ_{yy} of Fig. 8b correspond to positive and negative extrema in $\dot{x}_z$. Figure 8f shows the instantaneous turbulent shear stress component τ_{yz}. This stress component exhibits antisymmetry about the wake centerline; regions of strong z-momentum flux toward the wake centerline are separated by smaller regions of weaker z-momentum flux away from the centerline. One interesting feature of Fig. 8f is the relatively large stress associated with entrainment of freestream fluid into the regions between the large-scale structures. Another interesting feature can be observed by comparing the production of turbulent kinetic energy, Fig. 7c, with the instantaneous turbulent shear stress component τ_{yz}; we then observe that the extrema in τ_{yz} lies very close to the extrema in production and, thus, also close to the saddle points implying that production of kinetic energy of the fluctuating motion through the mechanism of vortex stretching increases the turbulent shear stress. The data displayed in Fig. 8 can also be used to compute the correlation coefficient for the fluctuating motion. The value obtained at the vortex centers are about one order of magnitude lower than the value obtain near the saddle points. It is, thus, clear that the large-scale turbulence is strongly coupled to the strain and the vorticity fields associated with the large-scale structures.

Concluding Remarks

In this paper a LES model for anisochoric flows has been suggested and investigated. Simulation results from the LES model, as well as from traditional RAS models, are compared with experimental measurements of unsteady wake flow around a two-dimensional generic triangular shaped bluff bodies at $10^3 < Re < 10^5$ and $0.01 < Ma < 0.20$. The simulation results are also used to investigate the mechanisms of the large-scale structures characterizing the flowfield.

The results obtained in this investigation with two-dimensional and, particularly, three-dimensional LES are in much better agreement with the experimental measurements than the results obtained with both the k–ε model and the DRSM. It is shown that two-dimensional LES cannot accurately mimic the actual physical processes in the flow, the three-dimensional LES, giving superior correlations between simulations and experiments, clearly indicates that such complex flows must be treated as fully three dimensional. The agreement between predicted and measured rms-velocity and turbulent shear stress profiles given in Figs. 5 and 6 and a continuous monitoring of the energy spectrum indicate that the major part of the turbulent motion has been resolved in the LES. From the energy spectrum it is observed that the main part of the kinetic energy of the fluctuating motion is contained in a wave number range between 200 and 300 m^{-1}. This corresponds to eddies of the characteristic size of 3–10 mm and indicates that the turbulent Reynolds number, based on the fluctuating streamwise velocity, the energy containing eddies, and the viscosity, is about $Re_T = 3500$.

Regarding the two different simulation approaches the following general comments can be put forward. Generally, RAS suffer from the following basic shortcomings: 1) When defining a time or ensemble averaged flow and considering fluctuations about the mean flow, there is some ambiguity about what it means to have time-dependent equations. Thus, a multiple time-scale approximation is implied. 2) In complex flows, where several components of the Reynolds stress tensor are of importance, the basic assumption of a scalar eddy viscosity appears too simple. The major drawback of LES is that fine grids are necessary, thus the simulations will be much more expensive than simulations using RAS. LES further suffers from two theoretical shortcomings: 1) lack of knowledge of how to formulate accurate SGS closure models and 2) the inaccurate treatment of the substantial time derivative of pressure and the dissipation function.

The concept of frame indifference can be a powerful tool in investigating the averaged and/or filtered equations of motion. The reason for not making systematic use of the concept of frame indifference in this paper is that a thorough investigation deserves a paper of its own. With the exception of the work of Speziale[32] few studies along these lines have been published. Frame indifference may be a valuable tool when formulating closure models for the SGS cross and Reynolds quantities and in investigating the character of the approximations made when deriving the filtered fluid dynamic equations in LES.

Acknowledgments

The author would like to thank the National Supercomputer Center (NSC) in Linköping, Sweden for providing the computational resources for the very extensive calculations, CHAM for providing us with the code Phoenics, version 2.0, in which the LES model and the numerics is implemented, and E. Lundgren and S.-I. Möller for valuable discussions.

References

[1]Lumley, J. L., "Turbulence Modeling," *ASME Journal of Applied Mechanics*, Vol. 50, 1983, p. 1097.

[2]Deardorff, J. W., "A Numerical Study of Three-Dimensional Turbulent Channel Flow at Large Reynolds Numbers," *Journal of Fluid Mechanics*, Vol. 41, 1970, p. 453.

[3]Truesdell, C., *A First Course in Rational Continuum Mechanics*, Academic, New York, 1977, p. 180.

[4]Yoshizawa, A., "Sub-Grid Scale Modeling of Compressible Turbulent Flow," *Physics of Fluids A*, Vol. 3, 1990, p. 714.

[5]Speziale, C. G., Erlebacher, G., Zang, T. A., and Hussaini, M. Y., "The Subgrid-Scale Modeling of Compressible Turbulence," *Physics of Fluids A*, Vol. 31, 1988, p. 940.

[6]Zang, T. A., Dahlburg, R. B., and Dahlburg, J. P., "Direct and Large-Eddy Simulations of Three Dimensional Compressible Navier–Stokes Turbulence," *Physics of Fluids A*, Vol. 4, 1992, p. 127.

[7]Erlebacher, G., Hussaini, M. Y., Speziale, C. G., and Zang, T. A, "Toward the Large-Eddy Simulation of Compressible Turbulent Flows," Inst. of Computer Applications in Science and Engineering, ICASE Rept. 187460, Hampton, VA, 1990.

[8]Sjunneson, A., Olovsson, S., and Sjöblom, B., "Validation Rig—A Tool for Flame Studies," VOLVO Flygmotor AB, Trollhättan, Sweden, 1991.

[9]Nagata, H., Kakehei, Y., Tsunekawa, M., and Hasegawa, T., *Bulletin of the Japan Society of Mechanical Engineers*, Vol. 18, 1975, p. 992.

[10]Franke, R., and Rodi, W., "Calculation of Vortex Shedding Past a Square Cylinder with Various Turbulence Models," *Eighth Symposium on Turbulent Shear Flows*, Munich, Germany, 1991, p. 20.1.1.

[11]Rodi, W., "On the Simulation of Turbulent Flow Past Bluff Bodies," First International Symposium on Comp. Wind Eng., Tokyo, Japan, Aug. 1992.

[12]Truesdell, C., and Noll, W., "The Non-Linear Field Theories of Mechanics," *Encyclopedia of Physics*, Vol. III/3, Springer, Berlin.

[13]Taylor, G. I., "Statistical Theory of Turbulence," *Proceedings of the Royal Society of London, A*, Vol. 151, 1935, p. 4.

[14]Pope, S. B., "The Statistical Theory of Turbulent Flames," *Philosophical Transactions of the Royal Society of London*, Vol. 291, 1978, p. 529.

[15]Boussinesq, J., "Essai sur la theorie des eaux courants," *Mem. pres. par div. sav. a l'Academie Sci.*, Paris, Vol. 23, 1877, p. 1.

[16]Jones, W. P., and Launder, B. E., "The Prediction of Laminarization with a Two-equation Model of Turbulence," *International Journal of Heat and Mass Transfer*, Vol. 15, 1971, p. 301.

[17]Speziale, C. G., and Sarkar, S., "Second-Order Closure Models for Supersonic Turbulent Flows," AIAA Paper 91-0217, 1991.

[18]Gibson, M. M., and Younis, B. A., "Calculation of Swirling Jets with a Reynolds Stress Closure," *Physics of Fluids A*, Vol. 29, 1986, p. 38.

[19]Cebeci, T., and Smith, A. M. O., *Analysis of Turbulent Boundary Layers*, Academic, New York, 1974.

[20]Reynolds, O., "On the Dynamical Theory of Incompressible Viscous Fluids and the Determination of the Criterion," *Philosophical Transactions of the Royal Society of London*, Vol. 186, 1895, p. 123.

[21]Leslie, D. C., and Quarini, G. L., "The Application of Turbulence Theory to the Formulation of Subgrid Modeling Procedures," *Journal of Fluid Mechanics*, Vol. 91, 1979, p. 65.

[22]Smagorinsky, J. S., "General Circulation Experiments with Primitive Equations," *Monthly Weather Review*, Vol. 91, 1963, p. 99.

[23]McMillan, O. J., and Ferziger, J. H., "Direct Testing of Subgrid Scale Models," *AIAA Journal*, Vol. 17, 1979, p. 1340.

[24]Schumann, U., "Ein Verfahren zur Direkten Numerischen Simulation Turbulenter Strömungen in Platten und Ringspaltkanälen und über seine Anwendung zur Untersuchung von Turbulenzmodellen," *Dissertation*, Univ. of Karlsruhe, KFK-1854, Karlsruhe, Germany, 1973.

[25]Deardorff, J. W., "Simulation of Turbulent Channel Flow," *Journal of Fluids Engineering,* Vol. 95, 1973, p. 429.

[26]Bardina, J., Ferziger, J. H., and Reynolds, W. C., "Improved Turbulence Models Based on Large-Eddy Simulation of Homogeneous, Incompressible Turbulent Flows," Stanford Univ., Rept. TF-19, Stanford, CA, 1983.

[27]Moin, P., and Kim, J., "Numerical Investigation of Turbulent Channel Flow," *Journal of Fluid Mechanics,* Vol. 118, 1981, p. 341.

[28]Gaskel, P. H., and Lau, A. K. C., "Curvature-compensated Convective Transport: SMART, A New Boundedness-preserving Transport Algorithm," *International Journal for Numerical Methods in Fluids,* Vol. 8, 1988, p. 617.

[29]Patankar, S. V., and Spalding, D. B., "A Calculation Procedure for Heat, Mass and Momentum Transfer in Three Dimensional Parabolic Flows," *International Journal of Heat and Mass Transfer,* Vol. 15, 1980, p. 1787.

[30]Gustafsson, B., and Sundström, A., "Incompletely Parabolic Problems in Fluid Dynamics," *SIAM Journal on Applied Mathematics,* Vol. 35, 1978, p. 343.

[31]Piomelli, U., Ferziger, J. H., Moin, P., and Kim, J., "New Approximate Boundary Conditions for Large Eddy Simulations of Wall-bounded Flows," *Physics of Fluids, A,* 1981, p. 1061.

[32]Speziale, C. G., "Galileian Invariance of Subgrid-scale Stress Models in the Large-Eddy Simulation of Turbulence," *Journal of Fluid Mechanics,* Vol. 156, 1985, p. 55.